Towards Data-efficient Mechanical Design of Bicontinuous Composites Using Generative AI

Milad Masrouri[1,2] *Zhao Qin*[1,2,3] *

1 Department of Civil and Environmental Engineering, Syracuse University, Syracuse, NY 13244, USA

2 Laboratory for Multiscale Material Modelling, Syracuse University, 151L Link Hall, Syracuse University, Syracuse, NY 13244, USA

3 The BioInspired Institute, Syracuse University, NY 13244, USA

*Materials & Correspondence should be addressed to Z.Q. (zqin02@syr.edu)

Abstract

The distribution of material phases is crucial to determine the composite's mechanical property. While the full structure-mechanics relationship of highly ordered material distributions can be studied with finite number of cases, this relationship is difficult to be revealed for complex irregular distributions, preventing design of such material structures to meet certain mechanical requirements. The noticeable developments of artificial intelligence (AI) algorithms in material design enables to detect the hidden structure-mechanics correlations which is essential for designing composite of complex structures. It is intriguing how these tools can assist composite design. Here, we focus on the rapid generation of bicontinuous composite structures together with the stress distribution in loading. We find that generative AI, enabled through fine-tuned Low Rank Adaptation models, can be trained with a few inputs to generate both synthetic composite structures and the corresponding von Mises stress distribution. The results show that this technique is convenient in generating massive composites designs with useful mechanical information that dictate stiffness, fracture and robustness of the material with one model, and such has to be done by several different experimental or simulation tests. This research offers valuable insights for the improvement of composite design with the goal of expanding the design space and automatic screening of composite designs for improved mechanical functions.

Keywords: Generative Artificial Intelligence, Stable Diffusion, composite design, phase field model, Molecular Dynamics Simulation

Composites are multi-phase materials made from two or more materials, which are typically in forms of a matrix and a reinforced material of distinct mechanical properties. Composites outperform traditional materials in many engineering areas, including aerospace [1], defense industry [2], automotive [3], healthcare [4], and construction [5]. The optimization of composite designs has become a key component in the development of materials in modern engineering applications since it enables the combination of multiple advanced mechanical functions that cannot be achieved by any individual component per se, e.g., stiffness [6], toughness [7], elasticity [8], ultimate strength [9], thermal conductivity [10]. Traditional manufacturing techniques have restricted the design and production of complex geometric arrangement of composite materials because of the challenges in effectively bonding two or more base materials with robust adhesion [11]. Thanks to the progress in additive manufacturing, however, it is now feasible to 3D print various materials. This enables the design and production of complex architectures in nature with diverse properties in all three spatial dimensions and with any geometry and combination of distinct materials [12]. Indeed, nature has provided many composite materials as examples for demonstrating the advantage of integrating multiple material phases, which have been refined over millions of years of evolution [13-14]. Nearly all natural materials exhibit composite structures, typically composed of a limited set of polymeric substances, including proteins or polysaccharides, as well as ceramic constituents or building blocks like calcium salts or silica, which are composites themselves [15-18]. For example, bone is a natural composite material that consists of a matrix primarily made of collagen, reinforced with the mineral hydroxyapatite, giving bone both strength and flexibility [19]. Other examples include nacre [20], a biomineral composite composed of calcium carbonate crystals embedded in an organic matrix, and bamboo [21], a natural composite consisting of cellulose fibers embedded in a lignin matrix, to name but a few. Principles derived from exceptional biological composites encompass: (i) the integration of rigid and soft materials for strength and toughness [22-24], (ii) the establishment of strong three-dimensional interconnections between phases to distribute loads and dissipate energy effectively [24-25], and (iii) the alignment of structurally anisotropic elements to enhance performance in specific orientations [26]. A bicontinuous composite structure, an interpenetrating phase composite (IPC) [27], can potentially fulfill all design criteria at the same time if it is constructed with a submicrometer-scale framework architecture [28]. A bicontinuous composite possesses a material structure characterized by the presence of two interconnected continuous phases, often with distinct properties. In these composites, both phases form a continuous network without being separated into distinct domains. This results in a complex and interconnected microstructure, where one phase is dispersed throughout the other in a way that maintains continuity [29]. This irregular material distribution can result in greater damage resistance as well as much more uniform deformation and gradual failure. The larger surface area at a given volume fraction of rigid phase results in increased matrix support on the load bearing. Moreover, the stochastic nature and

complex shape of these structures not only act as crack barriers and locally inhibit crack propagation, but also continue to provide load-bearing capacity even after fractures of some members occurs [30]. Bicontinuity arising from natural processes such as spinodal decomposition [31] can serve as a robust platform for the assembly of bicontinuous composite materials with tunable domain sizes across the nano and micrometer scales [32]. An example of this structure in nature is the dactyl club of mantis shrimps containing an impact-resistant coating composed of densely packed bicontinuous nanoparticles hydroxyapatite integrated within an organic matrix [33]. Li et al. introduced a 3D fiber-network-reinforced bicontinuous composite solid electrolyte holding great promise for enhancing the performance and safety of all-solid-state lithium metal batteries [34]. Sharifi et al. have proposed class of robust bicontinuous elastomer–LMPA foam composites with highly tunable mechanical stiffness [35]. Jiang et al. fabricated low-Young modulus, high satrength and biocompatible Ti-Mg composites with bicontinuous structure [36].

For materials use in a variety of engineering disciplines, reliable mechanical properties prediction, such as strength, stiffness, elasticity, plasticity, ductility, brittleness, toughness, and hardness, are of utmost importance [37]. Tensile, compression, and impact testing, among other time-consuming and expensive experimental techniques, have traditionally been used to evaluate the mechanical properties of materials[38-40]. Researchers and experts have increasingly resorted to simulation-based ways to predict mechanical properties [41]. Lin et al. adopted a physics-based coarse-grained model for silk proteins and applied the model to reveal the critical processing conditions and design parameters that control silk fiber assembly, demonstrating a de novo composites design [42]. Numerical simulations, as opposed to experimental measurements, have benefits like less equipment and material usage. However, the accuracy of the data generated by simulations may differ, and the calculations frequently call for high-performance computing resources. Recent times have seen a significant increase in the use of data-driven techniques thanks to the data generated by simulations and experiments alike [43]. Scientists have had good success forecasting material performance and design optimization using AI techniques because of developments in artificial intelligence and material informatics [11, 44-46]. Convolutional neural network (CNN) has been utilized by Gu et al. to predict the properties of composite materials and to create high-performance designs with significantly improved material properties compared to training data [47]. In another study, Gu et al employed CNN for the calculation and prediction of mechanical properties in composite materials, as well as for the optimization of designs [11]. Abueidda et al. extended the Gu et al.'s [11] study and integrated an optimization scheme based on genetic algorithm with a developed CNN model to optimize mechanical properties by considering factors like the volume fractions of rigid and flexible materials and their spatial distribution within the microstructure [48]. These approaches can study a composite system without complete characterization of its microstructure, accelerating the material

property prediction process. However, they are inherently data-intensive, meaning they require substantial amounts of labeled data to learn and make accurate predictions, and their performance is intricately tied to the quality and quantity of the training data [49]. However, Generative AI (GenAI) methods are valuable in scenarios where data is scarce as they alleviate data-intensiveness concerns. GenAI models can be trained and utilized to generate data effectively even with limited training data.

A type of artificial intelligence known as GenAI can produce a wide range of data, including images [50], videos [51], audio [52], text [53], and 3D models [54] in response to simple natural language prompts. It accomplishes this by identifying patterns in already collected data and using those patterns to create novel and distinctive outputs. GenAI operates by leveraging machine learning techniques, particularly deep learning, to create data that is coherent and novel. Its fundamental mechanism involves the use of neural networks, more specifically, Generative Adversarial Networks (GANs) [55]. GenAI employs a generator network, which is trained to produce data. This network starts with random noise and gradually refines its outputs to match the desired data distribution. A discriminator network assesses both the generated and real data concurrently, gaining the ability to discriminate between generated and real content. GenAI employs adversarial training, where the generator competes with the discriminator [55]. The generator's goal is to produce data that closely resembles real data, while the discriminator tries to enhance its ability to distinguish between genuine and synthetic content [56]. This competitive interaction results in the generator generating more realistic content. GenAI often utilizes a latent space, which is a lower-dimensional space where it can manipulate data. By exploring this space, the generator can create variations of the content it is generating, allowing for the generation of diverse and unique outputs [57]. Stable Diffusion, introduced in 2022, is a Markov chains trained text-to-image model that leverages latent diffusion [58-59], a deep learning technique, to create images from textual descriptions. In the Diffusion model, the general process involves introducing noise to the original image by adding Gaussian-distributed noise repeatedly until a fully noisy version is achieved. Subsequently, this noise is reversed to reconstruct the original image [60]. A schematic of Stable Diffusion models is shown in Fig. S1 in Supplementary Materials [61]. In contrast to GANs, which necessitate training against a discriminator, or Variational Autoencoders (VAEs), which require a variational posterior, estimating the loss of the diffusion model is notably straightforward. This simplicity and efficiency in training empower the diffusion model to excel in various tasks and disrupt the longstanding dominance of GANs in image synthesis [62]. Furthermore, a variety of large model fine-tuning approaches, including DreamBooth [63], Low Rank Adaptation (LoRA) [64], and Hypernetworks [65], have made it possible to personalize AI designs. LoRA enables the training of specific dense layers in a neural network indirectly. It achieves this by optimizing the rank decomposition matrices of these dense layers during adaptation, while retaining the pre-trained weights [64] (See the supplementary Materials).

Here, to efficiently generate composite design of complex material distribution and quick revealing its mechanical response in loading, we develop our own workflow by integrating physics-based models with GenAI. This workflow, as illustrated in Fig. 1, delineates the steps involved, including data set generation, GenAI model training, and model validation. We use a phase-field model to generate bicontinuous composites of complex material distribution and elastic network in molecular dynamics (MD) to simulate the mechanical response of the composite in loading. We, subsequently, create the stress field and use the results to fine-tune a Stable Diffusion model by training LoRA models. This workflow enables to rapidly generate bicontinuous composite structures and corresponding stress distribution when subjected to an external load. We demonstrate that the generated results are different from the training inputs and the stress field can be validated by the MD simulations. Our models are capable of massively generating composite designs with stress distribution, enabling the prediction of vulnerable areas, and leading to improved material design for enhanced mechanical properties.

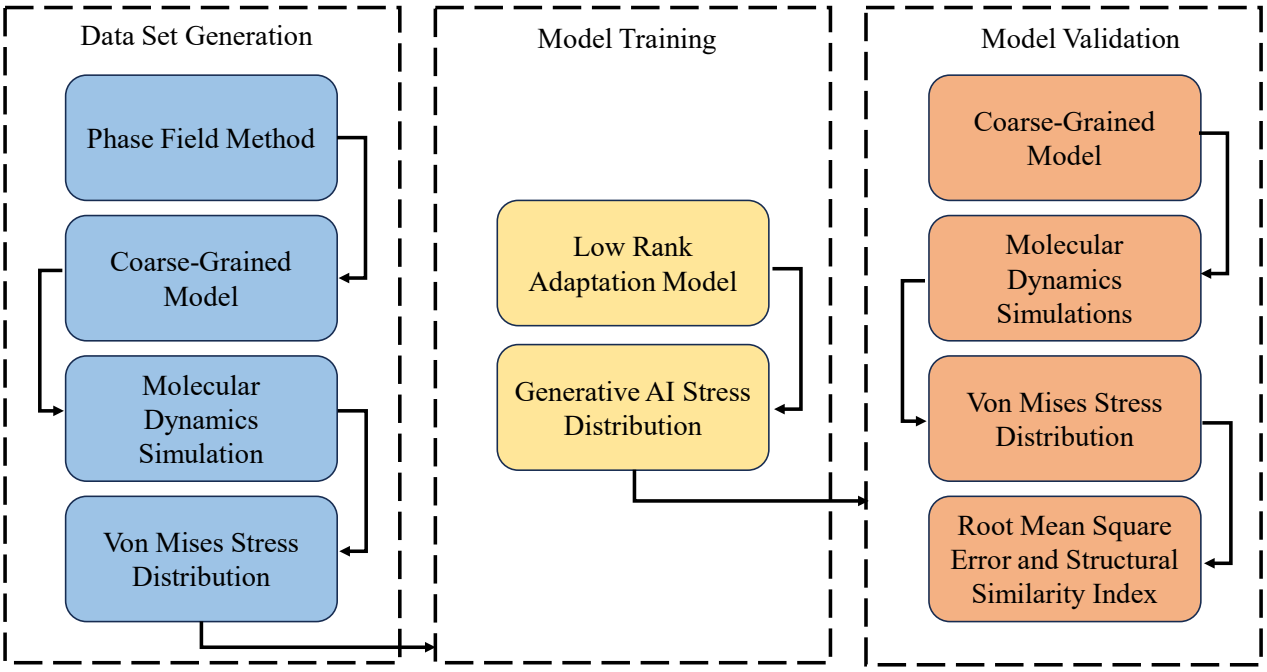

Fig. 1. Workflow of the Study: Data Set Generation, Model Training, and Model Validation.

We use phase field method [29] to simulate the diffusion and separation of binary composite melt mixture, allowing the two phases to initiate with a randomly mixed configuration and ultimately reach an equilibrium structure split into two phases with bicontinuous structure, each of which has distinct characteristics [66-67]. This simulation is enabled through the numerical solution of the Cahn-Hilliard equation [68] which is represented as:

$$\frac{\partial u}{\partial t} = \nabla^2[\frac{\mathrm{d}f(u)}{\mathrm{d}u} - \theta^2\nabla^2 u]\,. \quad (1)$$

In Eq. (1), -1<u< 1 represents the difference in concentration of the two phases, with u<0 denoting the soft and u≥0 representing the rigid phases. The function $f(u) = \frac{1}{4} - (u^2\text{-}1)^2$ characterizes the double-well free energy profile. The parameter θ controls the width of the transition region between two phases, akin to a diffusion coefficient of $\frac{[\text{length}]^2}{\sqrt{[\text{time}]}}$. The differential equation, when discretized and coupled with periodic boundary conditions in the x-y directions, allows for the simulation of the evolution of the two mixed phases within a 2D plane (For additional insights into the phase field model and the parameters employed, please consult the Supplementary Materials, and refer to Table S2).

Following the generation of structural models, we proceed to convert these models into coarse-grained molecular dynamics models, which are then utilized as input data for the LAMMPS package [69]. FEM-based phase field crystal modeling and Monte Carlo method have also been implemented for solid deformation and fracture simulation by researchers [70-73]. In our model, we treat each material phase as an arbitrary simple isotropic, homogenous solid material and the adopted elastic network is sufficient for the purpose with computational efficiency in data generation. It is important to acknowledge that the model operates in a non-equilibrium state; however, it exhibits computational efficiency and enables the simulation of dynamic interactions between materials and cracks. To represent the bicontinuous composite, we employ a simplified model consisting of a regular triangular mesh. In this model, each spring is described using a Morse potential, and the energy associated with these springs is calculated as follows:

$$E = D[1 - \mathrm{e}^{-\alpha(r-\alpha)}]^2\,. \quad (2)$$

Here, D and α are parameters related to the potential energy, and a represents the initial length of the spring, corresponding to the lattice constant of the triangular network. When considering the area of each mass bead, which acts as a node of the network, given by $\frac{\sqrt{3}}{2}\alpha^2$, and the fact that each bead is connected to three neighboring beads, the spring stiffness can be expresses as:

$$\frac{\mathrm{d}^2 E}{\mathrm{d}r^2}(r=\alpha) = 2D\alpha^2 = \frac{\sqrt{3}}{4}Et, \quad (3)$$

where E is the Young's modulus and t is the material thickness. The spring strength is determined by

$$\max\left(\frac{dE}{dr}\right) = \frac{1}{2} D\alpha = \frac{\sqrt{3}}{3}\sigma_c t\alpha, \tag{4}$$

where σ_c is the material ultimate strength. Using Eqs. (3) and (4), we can solve the potential parameters as:

$$\alpha = \frac{3E}{16\sigma_c \alpha} \text{ and } D = \frac{\frac{32\sqrt{3}}{9}\sigma_c^2 \alpha^2 t}{E}. \tag{5}$$

We summarize the numerical value of the potential parameters of the two material phases (rigid for Field's metal, a eutectic alloy of bismuth, indium, and tin; and soft for thermoelastic elastomer) in Table 1[74]. (To see more details of the model development see the Supplementary Materials)

Table 1: The numerical values of the potential parameters used in the computational simulations in LAMMPS.

Parameter	Rigid phase	Soft phase
Material thickness t (μm)	1	1
Young's modulus E (pg.μm^{-1}.ms^{-2})	10^7	3400
Ultimate strength σ_c (pg.μm^{-1}.ms^{-2})	33400	14000
Bond stiffness k (pg.μm^{-2})	4.33×10^6	1.472×10^3
Bond length a (μm)	0.373	0.373
Bond parameter α (1. μm^{-1})	150.5	0.122
Bond energy D (pg.μm^{-2}.ms^{-2})	95.6	49400

We use LAMMPS to perform Molecular Dynamics (MD) simulations using the Morse potential and micro units. Each sample is meticulously relaxed to its minimum energy configuration using the conjugate gradient method prior to the application of any external loads. After that, using a Nosé-Hoover thermostat, the samples are thermally equilibrated at 300 K for 40 μs. We use 2 ns as the time step and apply periodic boundary conditions in *x*-*y* dimensions. The simulation box is stretched with a constant strain rate (0.0001μs^{-1}) in the *y*-direction to create uniaxial tension as it is shown in Fig. 2. We utilize the OVITO software for the purpose of visualizing the structures following exposure to an external load, with the specific objective of illustrating the distribution of Von Mises stress. To create the dataset, we subject the structures to an external load for a duration of only 10 μs. This brief exposure allows us to observe the initial stress distribution under relatively low external loads and to remain in the elastic region.

We employ the Python library called "Kohya SS" for the purpose of training Low-Rank Adaptation (LoRA) models. LoRA is a training technique for fine-tuning Stable Diffusion models, specifically designed to be compatible with consumer-grade GPUs and seamlessly integrated with AUTOMATIC1111's web-based user interface. LoRA offers a good trade-off between file size and training power when compared to other training techniques like Dreambooth and textual inversion. LoRA applies small changes to the most critical part of Stable Diffusion models, the cross-attention layers [75]. It is the part of the model where the image and the prompt meet. Utilizing a LoRA model on its own is not viable; it must be employed in conjunction with a model checkpoint file. LoRA works by making subtle modifications to the accompanying model file, thereby influencing its attributes. We use stable-diffusion-v1-5 as the model checkpoint file and a learning rate of 0.001, coupled with a constant learning rate scheduler, is carefully selected to prevent the overlooking of intricate training details. The AdamW8bit optimizer is employed for the dynamic adaptation of the neural network throughout the process. Moreover, the Network Rank (dimension) is established at 128, specifying the quantity of neurons within the hidden layer of the additional small neural net. Network Alpha, which is introduced as a practical measure to avoid the rounding of weights to zero when saving the LoRA trained model, is set to be 1. LoRA, by design, tends to drive neural network weights towards smaller values, potentially reaching a point where they are practically indistinguishable from zero, implying the network is not learning effectively. To address this, a technique has been proposed in which the actual weight value stored is kept relatively large, but the weight is consistently attenuated at a constant rate during the learning process, giving the impression of a smaller weight value. These parameters are determined through a process of trial and error, involving a thorough comparison of the model's accuracy at each stage (See Table S1 in Supplementary Materials to find all the parameters used to train LoRA models in Kohya SS Python library).

The process of data set generation begins with the creation of 150 random models through the phase field method. In Fig. 2, an example of these structures is shown, with blue indicating the presence of rigid component and yellow denoting the soft phase. It is worth mentioning that in our 2*D* representation, the term bicontinuous is used to anticipate the inherently 3*D* and continuous nature of these structures in real-world applications. In a true 3*D* environment with ~50/50 phase A/phase B volume ratio, the two phases form a continuous and interconnected network. In this research, we build the models with a volume ratio of 55% rigid to 45% soft, resulting in the emergence of some soft inclusions (depicted in yellow) dispersed within the rigid matrix (depicted in blue). Figure 2a shows the stress strain curve of the structure subjected to an external tensile load in y direction for 10000 μs. Figure 2b and 2c display the structure configuration and stress distribution, respectively. Panels 1 through 6 are associated with the structure and stress distribution corresponding to the red dots on the stress-strain curve. Panel 4, which

illustrates the ultimate tensile strain, reveals the initiation and propagation of cracks within the structure. As we expect, the rigid phase can carry larger stresses compared to the soft phase. We use the elastic region of the stress-strain curve as the data set to train GenAI models capable of generating stress distribution images to predict how stress is distributed after the structure is subjected to a small load.

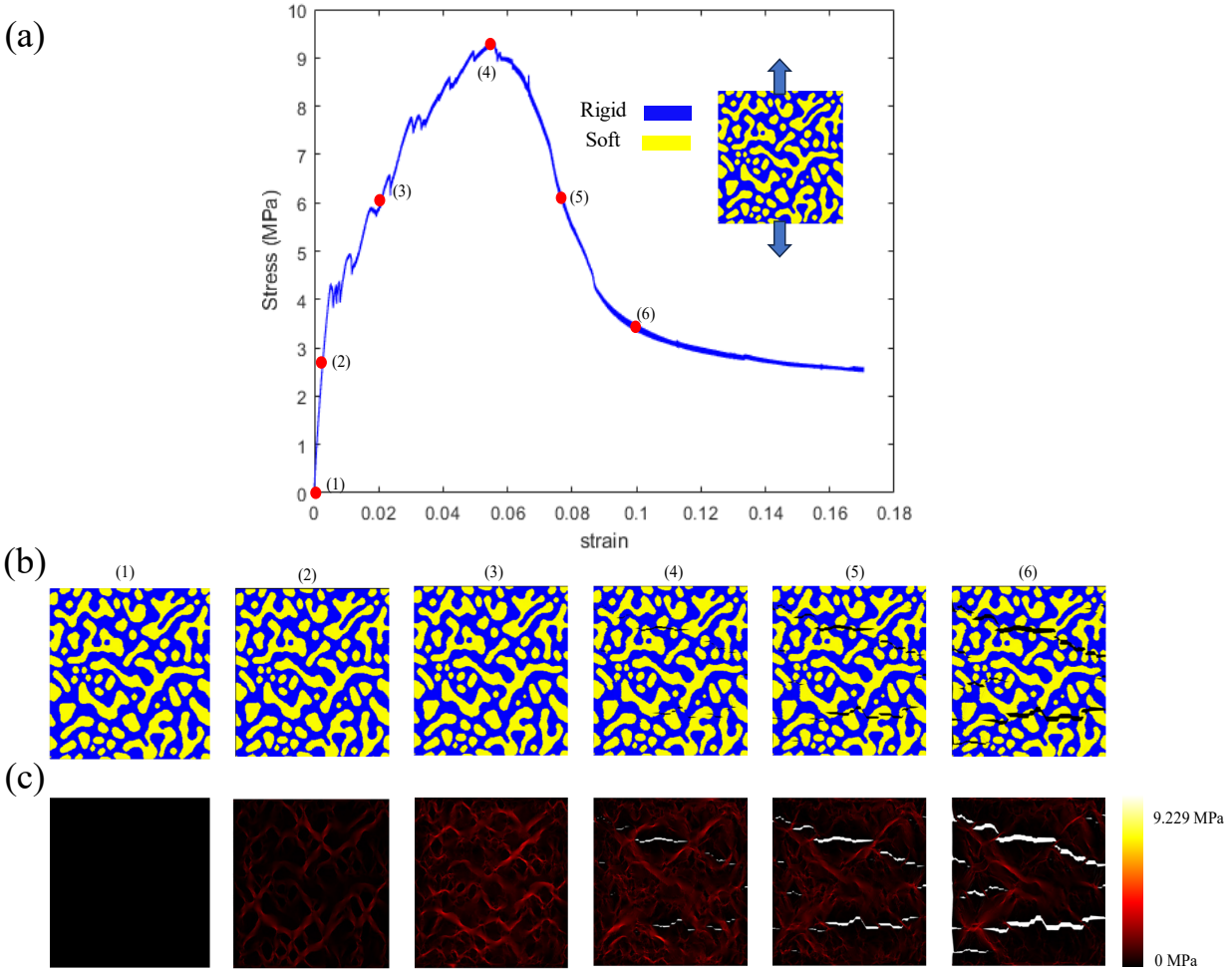

Figure 2. Mechanical properties of the bicontinuous composite structure from computational modeling for V_{rigid} = 55%, V_{soft} = 45% volume ratio (a) Stress-Strain curve from coarse-grained MD simulation. (b) Internal structure of the composites with different strain states (i.e., (1) $\varepsilon = 0$ (2) $\varepsilon = 0.002$ (3) $\varepsilon = 0.021$ (4) $\varepsilon = 0.058$ (5) $\varepsilon = 0.079$ (6) $\varepsilon = 0.1$) that correspond to the marks in panel (a) and (c) Von Mises stress distribution related to the corresponding strain levels shown by red dots on the curve.

We obtain 150 stress distribution images for the purpose of training the LoRA models, using subsets of 2, 5, 10, 25, 50, 100, 125, and 150 training images (i.e., model T2, T5, T10, T25, T50, T100, T125, T150, respectively). This approach is designed to assess how the quantity of training images impacts the accuracy of the GenAI models. The trained LoRA model is employed to generate synthetic images that

replicate the stress distribution in the random bicontinuous composite structures. As illustrated in Fig. 3, these GenAI-generated images are then transformed into a binary composite structure using image filtering techniques. Subsequently, these composite structures generated by GenAI are subjected to an external load within LAMMPS, after they have been converted into coarse-grained models. For evaluating the accuracy of the LoRA models, we employ pixel-wise root mean square deviation (RMSE) and the structural similarity index (SSIM). Pixel-wise RMSE serves as a metric for quantifying the dissimilarity between two images by computing the square root of the average of squared differences in pixel values. This calculation involves determining the squared difference in intensity values for corresponding pixels, reflecting the disparity in stress levels at those specific locations. The resulting single numerical value encapsulates the overall distinction in pixel intensities, offering a measure of how effectively one image aligns with the other in terms of stress intensity. Due to the absence of a specific RMSE threshold to be considered a good performance of the model, we include RMSE metric to enhance our ability to gain a nuanced understanding of the models' performance, aligning with the notion that a diverse set of metrics provides a more comprehensive assessment. SSIM is a metric for evaluating the perceived quality of two images by analyzing their structural information. Unlike pixel-wise RMSE, SSIM considers luminance, contrast, and structure in its assessment. The SSIM index is computed by analyzing mean, standard deviation, and cross-covariance for these components, ultimately providing an overall index that ranges from -1 to 1, where higher values indicate a greater level of structural similarity between the images. Figure 3 shows the comparison between the synthetic image (GenAI) and the real image (LAMMPS output) for 4 images. The pixel-wise difference map exhibits variations in stress distribution between the two images by contrasting the values of corresponding pixels. The normalized RMSE values demonstrate that the model exhibits a sufficient level of accuracy, making it suitable for predicting stress distribution within random bicontinuous composite structures However, it is important to note that the SSIM values, which quantify structural similarity, do not approach the desired level of 100% similarity (1). We assume that an SSIM higher than 0.5, when accompanied by a sufficiently small RMSE, indicates satisfactory alignment of stress.

Figure 3. Comparison between synthetic (GenAI) images and real (computational simulation output) images for model accuracy evaluation. The first two rows represent examples from the T100 model, while the last two rows are from the T50 model. All other parameters remain consistent for both models.

To assess the impact of the number of training images on the precision of the LoRA model, we undertake the training of LoRA models T2, T5, T10, T25, T50, T100, T125, T150. Subsequently, we generate 10 images with each model and repeat the model validation process for each individual image. We compute the SSIM matrix of the generated images and training images of T5, T50 and T100 as summarized in Fig. 4. It is shown that the generated image and training image have low SSIM, demonstrating that the new structures exhibit a remarkable degree of diversity and uniqueness, effectively mitigating the risk of mode collapse. Mode collapse, a known issue in generative models, often results in the limited generation of a repetitive set of outputs, thereby restricting exploration of the entire design space [76-77]. However, the outcomes presented in Fig. 4 provide compelling evidence that the SSIM values between any pair of generated images are consistently low, establishing the robustness of our model against mode collapse. This signifies the model's capacity to explore a broad and varied design landscape, fostering the generation of diverse and distinct structures, a crucial characteristic in generative modeling.

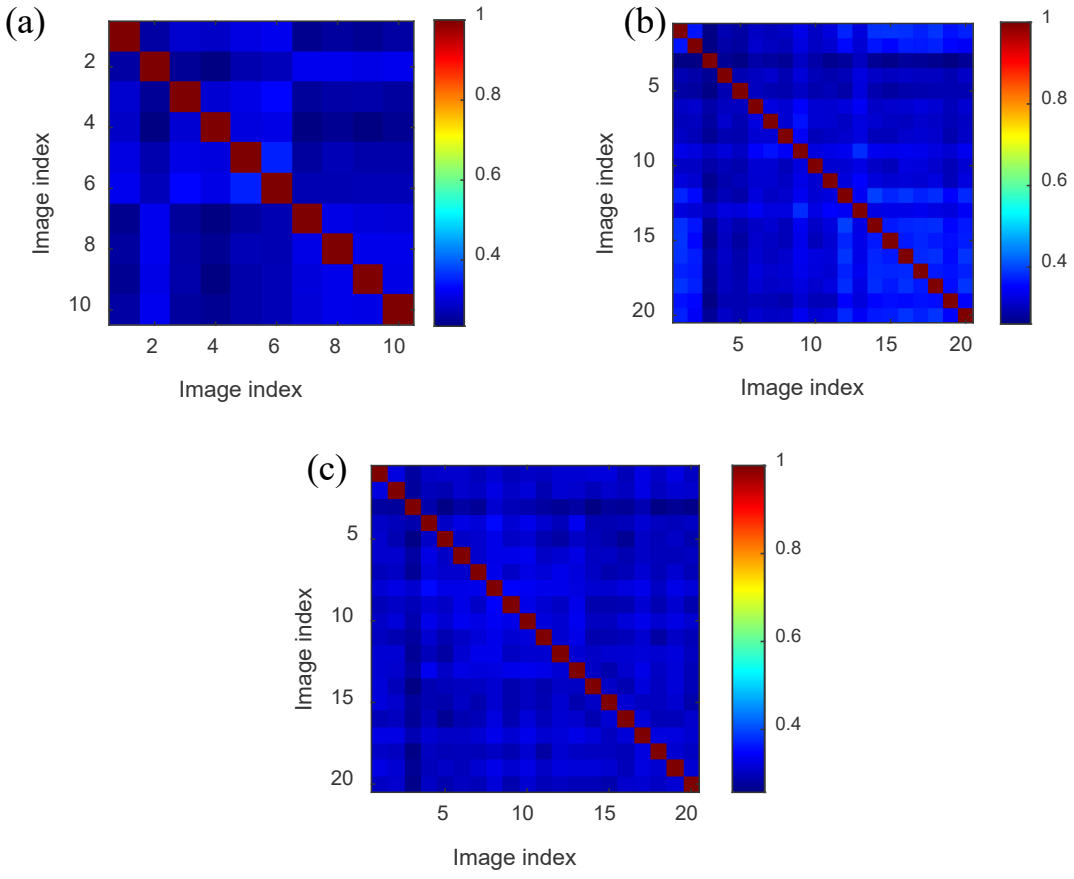

Figure 4. SSIM analysis of generated images and training images for (a) T5 (index ∈ [1,5] for generated, index ∈ [6,10] for training), (b) T50 (index ∈ [1,10] for generated, index ∈ [11,20] for training), and (c) T100 Models (index ∈ [1,10] for generated, index ∈ [11,20] for training).

In Fig. 5a, we present the RMSE and SSIM values for each model. Notably, the lowest RMSE value is observed T100, whereas the T125 model demonstrates the highest SSIM value. To select the most accurate model, we undertake a process of normalizing the RMSE and SSIM values and then calculate the aggregate error. Higher RMSE values denote heightened error levels, whereas lower SSIM values signify increased error. The combined error considers the normalized RMSE and SSIM values, standardizing them onto a uniform scale, for the computation of the overall error associated with each model. The combined error is calculated by Eq. (6).

$$Combined\ error = \omega_1 * RMSE_{\text{norm}} + \omega_2 * SSIM_{\text{norm}} \quad (6)$$

Where $RMSE_{\text{norm}} = (\frac{RMSE - \min(RMSE)}{\max(RMSE) - \min(RMSE)})$, $SSIM_{\text{norm}} = (\frac{\max(SSIM) - SSIM}{\max(SSIM) - \min(SSIM)})$, $\omega_1 = 0.5$ and $\omega_2 = 0.5$ denotes the weights of RMSE and SSIM respectively, showing the relative impact of RMSE and SSIM on the combined error. $RMSE_{norm}$ is a normalized term that gives the pixel-wise difference between true (LAMMPS output) images and synthetic (GenAI) images and has a value from 0 (identical) to 1 (very pixel-wisely different) for each generated design. $SSIM_{norm}$ is a normalized term that gives the overall difference between true (LAMMPS output) images and synthetic (GenAI) images and varies from 0 (identical) to 1 (very overall different). This normalization process allows for the fair assessment of the combination, ensuring that the lowest RMSE and the highest SSIM were represented by consistent values. We seek to determine the most favorable combination of RMSE and SSIM as a measure of accuracy of the models. We address this multi-objective decision-making by developing a combined error function that combines RMSE and SSIM errors. The objective is to minimize the combined error, which in practice means searching for a combination that achieves the lowest RMSE while maximizing SSIM simultaneously. Figure 5b shows the combined error for each model, indicating that T100 has the lowest combined error. This outcome signifies that T100 exhibits the highest level of accuracy. Achieving this level of accuracy with only 100 training images highlights the significant advantages of our approach compared to the CNN method. For instance, Yang et al. required a massive dataset of 26,000 training composite configurations to achieve acceptable accuracy when using the CNN method to predict the structure-mechanics correlation in composites [78]. Gu et al. generated 80,000 random microstructures as the training data to optimize the toughness of the hierarchical composite systems employing CNN [47]. Mann et. Al used 12,800 training configurations to capture highly non-linear microstructure-property in high contrast composite material systems by developing a new CNN architecture [79]. These numbers are orders of magnitude larger that the size of data set we use. While our method focuses on predicting stress distribution in various bicontinuous composites, as opposed to the studies mentioned that predict mechanical properties, we are optimistic that our approach has the potential to pave the way for the development of data-efficient methods for predicting the correlation between mechanics and structure.

We also observe that T2 model, using just 2 training images, can produce stress fields and composite structures although they exhibit lower accuracy compared to the T100 model. T2 model struggles to predict stress concentration regions within the stress field but is proficient in showing the overall Von Mises stress distribution in both rigid and soft phases. This distinction underscores the significance of our model, which can achieve its performance with just two training images, highlighting its efficiency and non-dependence on extensive data.

(a) (b)

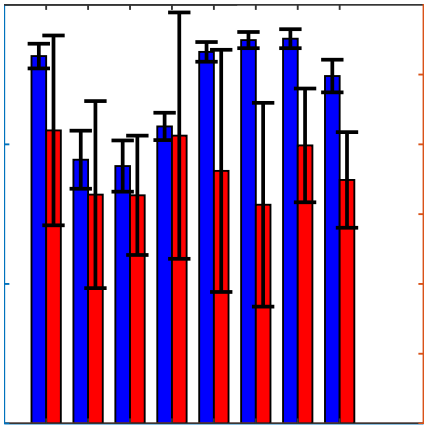

Figure 5. Comparison of (a) normalized RMSE and SSIM and (b) Combined scores obtained from scoring function for the models with different number of training images, computed with Eq. (6). All other hyperparameters such as optimizer type, learning rate, network architecture remains the same for different models.

In this study, using a combination of computational modeling and GenAI, we trained LoRA models to generate images that predict stress distribution in the bicontinuous composite structures separated by phase field method. The findings demonstrate the capability of this method to train proficient models for generating stress distribution predictions in random bicontinuous composites. This work provides significant insights to enhance composite design, with a focus on improving mechanical properties, all achieved without the necessity for conducting an extensive array of experimental or simulation tests. Instead, the outcomes are realized through the exclusive utilization of generative AI models. Our future endeavors involve the creation of data-efficient techniques that go beyond predicting stress distribution and extend to predicting the mechanics-structure correlation within composite structures, utilizing GenAI.

Author Contributions

Z.Q. proposed, designed the research scope and MD algorithm, and supervised the research. M.M. prepared the composite samples, performed the mechanical simulations, analysis the results and train the generative AI models. M.M. analyzed the simulation results, built the generative models, and performed the prediction. M.M. and Z.Q. wrote the manuscript, revised, and approved the manuscript.

Declaration of Interests

The authors declare no competing interests.

Acknowledgment

The authors acknowledge the National Science Foundation CAREER Grant (Award #: 2145392), the startup funding at Syracuse University for supporting the research work.

References

[1] C. Barile, C. Casavola, F. De Cillis, Mechanical comparison of new composite materials for aerospace applications, Compos B Eng. 162 (2019) 122–128. https://doi.org/10.1016/j.compositesb.2018.10.101.

[2] M. Maria, Advanced composite materials of the future in aerospace industry, Incas Bulletin. 5 (2013) 139–150. https://doi.org/10.13111/2066-8201.2013.5.3.14.

[3] M. Patel, B. Pardhi, S. Chopara, M. Pal, Lightweight Composite Materials for Automotive -A Review Lightweight Composite Materials for Automotive - A Review, International Research Journal of Engineering and Technology (IRJET). (2020) 41–47.

[4] M. Shwartz, J.D. Restuccia, A.K. Rosen, Composite Measures of Health Care Provider Performance: A Description of Approaches, Milbank Quarterly. 93 (2015) 788–825. https://doi.org/10.1111/1468-0009.12165.

[5] M. Jones, A. Mautner, S. Luenco, A. Bismarck, S. John, Engineered mycelium composite construction materials from fungal biorefineries: A critical review, Mater Des. 187 (2020) 108397. https://doi.org/10.1016/j.matdes.2019.108397.

[6] T. Sain, J. Meaud, G. Hulbert, E.M. Arruda, A.M. Waas, Simultaneously high stiffness and damping in a class of wavy layered composites, Compos Struct. 101 (2013) 104–110. https://doi.org/10.1016/j.compstruct.2013.01.024.

[7] D. Quan, R. Alderliesten, C. Dransfeld, N. Murphy, A. Ivanković, R. Benedictus, Enhancing the fracture toughness of carbon fibre/epoxy composites by interleaving hybrid meltable/non-meltable thermoplastic veils, Compos Struct. 252 (2020). https://doi.org/10.1016/j.compstruct.2020.112699.

[8] Q.D. To, M.T. Nguyen, G. Bonnet, V. Monchiet, V.T. To, Overall elastic properties of composites from optimal strong contrast expansion, Int J Solids Struct. 120 (2017) 245–256. https://doi.org/10.1016/j.ijsolstr.2017.05.006.

[9] Y. Pu, Z. Ma, L. Liu, Y. Bai, Y. Huang, Improvement on strength and toughness for CFRPs by construction of novel “soft-rigid” interface layer, Compos B Eng. 236 (2022) 109846. https://doi.org/10.1016/j.compositesb.2022.109846.

[10] A. Shimamura, Y. Hotta, H. Hyuga, M. Hotta, K. Hirao, Improving the thermal conductivity of epoxy composites using a combustion-synthesized aggregated β-Si3N4 filler with randomly oriented grains, Sci Rep. 10 (2020) 1–9. https://doi.org/10.1038/s41598-020-71745-w.

[11] G.X. Gu, C.T. Chen, M.J. Buehler, De novo composite design based on machine learning algorithm, Extreme Mech Lett. 18 (2018) 19–28. https://doi.org/10.1016/j.eml.2017.10.001.

[12] O. Diegel, A. Nordin, D. Motte, Additive Manufacturing Technologies, 2019. https://doi.org/10.1007/978-981-13-8281-9_2.

[13] R. Cartwright, Book Reviews: Book Reviews, Perspect Public Health. 130 (2010) 239–239. https://doi.org/10.1177/1757913910379198.

[14] A.R. Studart, Biological and bioinspired composites with spatially tunable heterogeneous architectures, Adv Funct Mater. 23 (2013) 4423–4436. https://doi.org/10.1002/adfm.201300340.

[15] J.F.V. Vincent, Biomimetic materials, J Mater Res. 23 (2008) 3140–3147. https://doi.org/10.1557/jmr.2008.0380.

[16] L. Li, C. Ortiz, Pervasive nanoscale deformation twinning as a catalyst for efficient energy dissipation in a bioceramic armour, Nat Mater. 13 (2014) 501–507. https://doi.org/10.1038/nmat3920.

[17] J.W.C. Dunlop, P. Fratzl, Biological composites, Annu Rev Mater Res. 40 (2010) 1–24. https://doi.org/10.1146/annurev-matsci-070909-104421.

[18] J. Aizenberg, P. Fratzl, Biological and biomimetic materials, Advanced Materials. 21 (2009) 387–388. https://doi.org/10.1002/adma.200803699.

[19] S. Weiner, H.D. Wagner, The material bone: Structure-mechanical function relations, Annual Review of Materials Science. 28 (1998) 271–298. https://doi.org/10.1146/annurev.matsci.28.1.271.

[20] C. Chun-Teh, J.M.-M. Francisco, L. Shengjie, Q. Zhao, J.B. Markus, Nacre-inspired design of graphene oxide–polydopamine nanocomposites for enhanced mechanical properties and multi-functionalities, Nano Futures. 1 (2017) 11003.

[21] D. Liu, J. Song, D.P. Anderson, P.R. Chang, Y. Hua, Bamboo fiber and its reinforced composites: Structure and properties, Cellulose. 19 (2012) 1449–1480. https://doi.org/10.1007/s10570-012-9741-1.

[22] K. Tai, M. Dao, S. Suresh, A. Palazoglu, C. Ortiz, Nanoscale heterogeneity promotes energy dissipation in bone, Nat Mater. 6 (2007) 454–462. https://doi.org/10.1038/nmat1911.

[23] X. Li, W.C. Chang, Y.J. Chao, R. Wang, M. Chang, Nanoscale structural and mechanical characterization of a natural nanocomposite material: The shell of red abalone, Nano Lett. 4 (2004) 613–617. https://doi.org/10.1021/nl049962k.

[24] A. Tanay, L. Bitincka, R. Shamir, E.K.O. Shea, A.I. Tschumi, R. Kishony, C.A. Telmer, S.A. Adler, C.A. Telmer, V. Subramaniam, A.J. Lopez, T.J. Mitchison, N. Perrimon, S.E. Fraser, J. Ellenberg, A.I. Lamond, J.S. Brotman, S.T. Sweeney, G. Davis, R. Daneman, M. Zavortink, W. Chia, L.F. Liu, P.D. Arpa, W.P. Pfund, V.B. Mehta, D.K. Trask, D. Makonchuk, C. Gomes, J.J. Zheng, M. Hetman, M.S. Wold, J.A. Borowiec, T.C. Elston, W.J. Blake, J.J. Collins, A.J. Levine, E.D. Siggia, P.S. Swain, M. Thattai, I. Kurtser, A.D. Grossman, A. Van Oudenaarden, S.J. Arlander, L. Karnitz, C. Lin, S.Y. Sun, S. Zhao, Z.R. Liu, W.M. Old, K.A. Resing, N.G. Ahn, M. Mann, J. Bar, I. Glinert, T. Shlapok, Tough, Bio-Inspired Hybrid Materials, (2008) 1516–1521.

[25] L. Han, L. Wang, J. Song, M.C. Boyce, C. Ortiz, Direct quantification of the mechanical anisotropy and fracture of an individual exoskeleton layer via uniaxial compression of micropillars, Nano Lett. 11 (2011) 3868–3874. https://doi.org/10.1021/nl201968u.

[26] B.J.F. Bruet, J. Song, M.C. Boyce, C. Ortiz, Materials design principles of ancient fisharmour, Nat Mater. 7 (2008) 748–756. https://doi.org/10.1038/nmat2231.

[27] D.R. Clarke, Interpenetrating Phase Composites, Journal of the American Ceramic Society. 75 (1992) 739–758. https://doi.org/https://doi.org/10.1111/j.1151-2916.1992.tb04138.x.

[28] J.H. Lee, L. Wang, S. Kooi, M.C. Boyce, E.L. Thomas, Enhanced energy dissipation in periodic epoxy nanoframes, Nano Lett. 10 (2010) 2592–2597. https://doi.org/10.1021/nl1012773.

[29] X.Y. Sun, G.K. Xu, X. Li, X.Q. Feng, H. Gao, Mechanical properties and scaling laws of nanoporous gold, J Appl Phys. 113 (2013). https://doi.org/10.1063/1.4774246.

[30] Y. Zhang, M.T. Hsieh, L. Valdevit, Mechanical performance of 3D printed interpenetrating phase composites with spinodal topologies, Compos Struct. 263 (2021) 113693. https://doi.org/10.1016/j.compstruct.2021.113693.

[31] K. Binder, D. Stauffer, Theory for the slowing down of the relaxation and spinodal decomposition of binary mixtures, Phys Rev Lett. 33 (1974) 1006–1009. https://doi.org/10.1103/PhysRevLett.33.1006.

[32] M.N. Lee, A. Mohraz, Bicontinuous macroporous materials from bijel templates, Advanced Materials. 22 (2010) 4836–4841. https://doi.org/10.1002/adma.201001696.

[33] W. Huang, M. Shishehbor, N. Guarín-Zapata, N.D. Kirchhofer, J. Li, L. Cruz, T. Wang, S. Bhowmick, D. Stauffer, P. Manimunda, K.N. Bozhilov, R. Caldwell, P. Zavattieri, D. Kisailus, A natural impact-resistant bicontinuous composite nanoparticle coating, Nat Mater. 19 (2020) 1236–1243. https://doi.org/10.1038/s41563-020-0768-7.

[34] D. Li, L. Chen, T. Wang, L.Z. Fan, 3D Fiber-Network-Reinforced Bicontinuous Composite Solid Electrolyte for Dendrite-free Lithium Metal Batteries, ACS Appl Mater Interfaces. 10 (2018) 7069–7078. https://doi.org/10.1021/acsami.7b18123.

[35] S. Sharifi, A. Mohammadi Nasab, P.E. Chen, Y. Liao, Y. Jiao, W. Shan, Robust Bicontinuous Elastomer–Metal Foam Composites with Highly Tunable Stiffness, Adv Eng Mater. 24 (2022). https://doi.org/10.1002/adem.202101533.

[36] S. Jiang, L.J. Huang, Q. An, L. Geng, X.J. Wang, S. Wang, Study on titanium-magnesium composites with bicontinuous structure fabricated by powder metallurgy and ultrasonic infiltration, J Mech Behav Biomed Mater. 81 (2018) 10–15. https://doi.org/10.1016/j.jmbbm.2018.02.017.

[37] L. Song, D. Wang, X. Liu, A. Yin, Z. Long, Prediction of mechanical properties of composite materials using multimodal fusion learning, Sens Actuators A Phys. 358 (2023) 114433. https://doi.org/10.1016/j.sna.2023.114433.

[38] M. Masrouri, G. Faraji, M.S. Pedram, M. Sadrkhah, In-vivo study of ultrafine-grained CP-Ti dental implants surface modified by SLActive with excellent wettability, Int J Adhes Adhes. 102 (2020) 102684. https://doi.org/10.1016/j.ijadhadh.2020.102684.

[39] J. Ni, S. Lin, Z. Qin, D. Veysset, X. Liu, Y. Sun, A.J. Hsieh, R. Radovitzky, K.A. Nelson, X. Zhao, Strong fatigue-resistant nanofibrous hydrogels inspired by lobster underbelly, Matter. 4 (2021) 1919–1934. https://doi.org/10.1016/j.matt.2021.03.023.

[40] L. Yang, Z. Qin, Experimental Analysis of the Mechanics of Mycelium-based Biocomposites, Bioprospects of Macrofungi: Recent Developments. (2023) 205–232. https://doi.org/10.1201/9781003343806-13.

[41] M. Masrouri, Z. Qin, Effects of terminal tripeptide units on mechanical properties of collagen triple helices, Extreme Mech Lett. 64 (2023) 102075. https://doi.org/10.1016/j.eml.2023.102075.

[42] S. Lin, S. Ryu, O. Tokareva, G. Gronau, M.M. Jacobsen, W. Huang, D.J. Rizzo, D. Li, C. Staii, N.M. Pugno, J.Y. Wong, D.L. Kaplan, M.J. Buehler, Predictive modelling-based design and experiments for synthesis and spinning of bioinspired silk fibres, Nat Commun. 6 (2015). https://doi.org/10.1038/ncomms7892.

[43] A. Stoll, P. Benner, Machine learning for material characterization with an application for predicting mechanical properties, GAMM Mitteilungen. 44 (2021) 2023. https://doi.org/10.1002/gamm.202100003.

[44] A. Sharma, T. Mukhopadhyay, S.M. Rangappa, S. Siengchin, V. Kushvaha, Advances in Computational Intelligence of Polymer Composite Materials: Machine Learning Assisted Modeling, Analysis and Design, Springer Netherlands, 2022. https://doi.org/10.1007/s11831-021-09700-9.

[45] U.M.R. Paturi, S. Cheruku, N.S. Reddy, The Role of Artificial Neural Networks in Prediction of Mechanical and Tribological Properties of Composites—A Comprehensive Review, Springer Netherlands, 2022. https://doi.org/10.1007/s11831-021-09691-7.

[46] J. Wei, X. Chu, X.Y. Sun, K. Xu, H.X. Deng, J. Chen, Z. Wei, M. Lei, Machine learning in materials science, InfoMat. 1 (2019) 338–358. https://doi.org/10.1002/inf2.12028.

[47] G.X. Gu, C.T. Chen, D.J. Richmond, M.J. Buehler, Bioinspired hierarchical composite design using machine learning: Simulation, additive manufacturing, and experiment, Mater Horiz. 5 (2018) 939–945. https://doi.org/10.1039/c8mh00653a.

[48] D.W. Abueidda, M. Almasri, R. Ammourah, U. Ravaioli, I.M. Jasiuk, N.A. Sobh, Prediction and optimization of mechanical properties of composites using convolutional neural networks, Compos Struct. 227 (2019) 111264. https://doi.org/10.1016/j.compstruct.2019.111264.

[49] D. Han, Q. Liu, W. Fan, A new image classification method using CNN transfer learning and web data augmentation, Expert Syst Appl. 95 (2018) 43–56. https://doi.org/10.1016/j.eswa.2017.11.028.

[50] H. Vartiainen, M. Tedre, Using artificial intelligence in craft education: crafting with text-to-image generative models, Digital Creativity. 34 (2023) 1–21. https://doi.org/10.1080/14626268.2023.2174557.

[51] N. Aldausari, A. Sowmya, N. Marcus, G. Mohammadi, Video Generative Adversarial Networks: A Review, ACM Comput Surv. 55 (2023). https://doi.org/10.1145/3487891.

[52] K. Lakhotia, E. Kharitonov, W.N. Hsu, Y. Adi, A. Polyak, B. Bolte, T.A. Nguyen, J. Copet, A. Baevski, A. Mohamed, E. Dupoux, On generative spoken language modeling from raw audio, Trans Assoc Comput Linguist. 9 (2021) 1336–1354. https://doi.org/10.1162/tacl_a_00430.

[53] H. Abburi, M. Suesserman, N. Pudota, B. Veeramani, E. Bowen, S. Bhattacharya, Generative AI Text Classification using Ensemble LLM Approaches, (2023) 1–8.

[54] S. Chaudhuri, D. Ritchie, J. Wu, K. Xu, H. Zhang, Learning Generative Models of 3D Structures, Computer Graphics Forum. 39 (2020) 643–666. https://doi.org/10.1111/cgf.14020.

[55] A. Creswell, T. White, V. Dumoulin, K. Arulkumaran, B. Sengupta, A.A. Bharath, Generative Adversarial Networks: An Overview, IEEE Signal Process Mag. 35 (2018) 53–65. https://doi.org/10.1109/MSP.2017.2765202.

[56] K. Wang, C. Gou, Y. Duan, Y. Lin, X. Zheng, F.Y. Wang, Generative adversarial networks: Introduction and outlook, IEEE/CAA Journal of Automatica Sinica. 4 (2017) 588–598. https://doi.org/10.1109/JAS.2017.7510583.

[57] J. Gui, Z. Sun, Y. Wen, D. Tao, J. Ye, A Review on Generative Adversarial Networks: Algorithms, Theory, and Applications, IEEE Trans Knowl Data Eng. 35 (2023) 3313–3332. https://doi.org/10.1109/TKDE.2021.3130191.

[58] R. Rombach, A. Blattmann, D. Lorenz, P. Esser, B. Ommer, Stable Diffusion, Cvpr. 2022-June (2022) 10674–10685.

[59] J. Ho, A. Jain, P. Abbeel, Denoising diffusion probabilistic models, Adv Neural Inf Process Syst. 2020-December (2020) 1–12.

[60] Z. Shi, AI Application to Generate an Expected Picture Using Keywords with Stable Diffusion, Journal of Artificial Intelligence Practice. 6 (2023) 66–71. https://doi.org/10.23977/jaip.2023.060110.

[61] R. Rombach, A. Blattmann, D. Lorenz, P. Esser, B. Ommer, High-Resolution Image Synthesis with Latent Diffusion Models, Proceedings of the IEEE Computer Society Conference on Computer Vision and Pattern Recognition. 2022-June (2022) 10674–10685. https://doi.org/10.1109/CVPR52688.2022.01042.

[62] L. Yang, Z. Zhang, Y. Song, S. Hong, R. Xu, Y. Zhao, W. Zhang, B. Cui, M.-H. Yang, Diffusion Models: A Comprehensive Survey of Methods and Applications, 1 (2022).

[63] N. Ruiz, Y. Li, V. Jampani, Y. Pritch, M. Rubinstein, K. Aberman, DreamBooth: Fine Tuning Text-to-Image Diffusion Models for Subject-Driven Generation, (2023) 22500–22510. https://doi.org/10.1109/cvpr52729.2023.02155.

[64] E. Hu, Y. Shen, P. Wallis, Z. Allen-Zhu, Y. Li, S. Wang, L. Wang, W. Chen, Lora: Low-Rank Adaptation of Large Language Models, ICLR 2022 - 10th International Conference on Learning Representations. (2022) 1–26.

[65] D. Ha, A.M. Dai, Q. V. Le, Hypernetworks, 5th International Conference on Learning Representations, ICLR 2017 - Conference Track Proceedings. (2017). https://doi.org/10.1142/9781860949739_0006.

[66] J.F. Rodriguez-Nieva, E.M. Bringa, T.A. Cassidy, R.E. Johnson, A. Caro, M. Fama, M.J. Loeffler, R.A. Baragiola, D. Farkas, Sputtering from a porous material by penetrating ions, Astrophysical Journal Letters. 743 (2011). https://doi.org/10.1088/2041-8205/743/1/L5.

[67] D.A. Crowson, D. Farkas, S.G. Corcoran, Geometric relaxation of nanoporous metals: The role of surface relaxation, Scr Mater. 56 (2007) 919–922. https://doi.org/10.1016/j.scriptamat.2007.02.017.

[68] J.W. Cahn, J.E. Hilliard, Free energy of a nonuniform system. I. Interfacial free energy, J Chem Phys. 28 (1958) 258–267. https://doi.org/10.1063/1.1744102.

[69] S. Plimpton, Fast Parasllel Algorithms for Short-Range Molecular Dynamics, Soft Matter. 14 (1994) 2–19. https://doi.org/10.1039/c7sm02429k.

[70] N. Noii, A. Khodadadian, F. Aldakheel, Probabilistic failure mechanisms via Monte Carlo simulations of complex microstructures, Comput Methods Appl Mech Eng. 399 (2022) 115358. https://doi.org/10.1016/j.cma.2022.115358.

[71] J.R. Mianroodi, P. Shanthraj, C. Liu, S. Vakili, S. Roongta, N.H. Siboni, N. Perchikov, Y. Bai, B. Svendsen, F. Roters, D. Raabe, M. Diehl, Modeling and simulation of microstructure in metallic systems based on multi-physics approaches, NPJ Comput Mater. 8 (2022) 1–15. https://doi.org/10.1038/s41524-022-00764-0.

[72] Z. Chen, Y. Hu, X. He, T. Xiao, L. Hao, Y. Ruan, Phase-field crystal method for multiscale microstructures with cubic term, Mater Today Commun. 29 (2021). https://doi.org/10.1016/j.mtcomm.2021.102935.

[73] A. Nourian-Avval, E. Asadi, On the quantification of phase-field crystals model for computational simulations of solidification in metals, Comput Mater Sci. 128 (2017) 294–301. https://doi.org/10.1016/j.commatsci.2016.11.042.

[74] J. Bu, N. Shen, Z. Qin, Integration of low-melting-point alloys and thermoplastic elastomers for 3D printing of multifunctional composites Integration of low-melting-point alloys and thermoplastic elastomers for 3D printing, Cell Rep Phys Sci. 4 (2023) 101604. https://doi.org/10.1016/j.xcrp.2023.101604.

[75] E. Hu, Y. Shen, P. Wallis, Z. Allen-Zhu, Y. Li, S. Wang, L. Wang, W. Chen, Lora: Low-Rank Adaptation of Large Language Models, ICLR 2022 - 10th International Conference on Learning Representations. (2022) 1–26.

[76] R. Durall, A. Chatzimichailidis, P. Labus, J. Keuper, Combating mode collapse in GAN Training: An empirical analysis using hessian eigenvalues, VISIGRAPP 2021 - Proceedings of the 16th International Joint Conference on Computer Vision, Imaging and Computer Graphics Theory and Applications. 4 (2021) 211–218. https://doi.org/10.5220/0010167902110218.

[77] D. Shu, J. Cunningham, G. Stump, S.W. Miller, M.A. Yukish, T.W. Simpson, C.S. Tucker, 3D Design Using Generative Adversarial Networks and Physics-Based Validation, Journal of Mechanical Design. 142 (2020) 1–15. https://doi.org/10.1115/1.4045419.

[78] F. Kibrete, T. Trzepieciński, H.S. Gebremedhen, D.E. Woldemichael, Artificial Intelligence in Predicting Mechanical Properties of Composite Materials, Journal of Composites Science. 7 (2023) 364. https://doi.org/10.3390/jcs7090364.

[79] A. Mann, S.R. Kalidindi, Development of a Robust CNN Model for Capturing Microstructure-Property Linkages and Building Property Closures Supporting Material Design, Front Mater. 9 (2022) 1–14. https://doi.org/10.3389/fmats.2022.851085.